# Inflammatory reaction in the retina after focal non-convulsive status epilepticus in mice investigated with high resolution magnetic resonance and diffusion tensor imaging

Ahl, Matilda; Lindbäck, Una; Chary, Karthic ; Shibata, Keisuke ; Chugh, Deepti; Linden Mickelsson, Pernilla; Kettunen, Mikko; COMPAGNO STRANDBERG, MARIA; Englund Johansson, Ulrica; Sierra, Alejandra; Ekdahl, Christine T

*Published in:*
Epilepsy Research

*DOI:*
10.1016/j.eplepsyres.2021.106730

2021

*Document Version:*
Publisher's PDF, also known as Version of record

Epilepsy Research 176 (2021) 106730

Contents lists available at ScienceDirect

Epilepsy Research

journal homepage: www.elsevier.com/locate/epilepsyres

# Inflammatory reaction in the retina after focal non-convulsive status epilepticus in mice investigated with high resolution magnetic resonance and diffusion tensor imaging

Matilda Ahl [a,b], Una Avdic [a,b], Karthik Chary [c], Keisuke Shibata [a,b], Deepti Chugh [a,b], Pernilla Lindén Mickelsson [a], Mikko Kettunen [c], Maria Compagno Strandberg [d], Ulrica Englund Johansson [e], Alejandra Sierra [c], Christine T. Ekdahl [a,b,*]

[a] Division of Clinical Neurophysiology, Sweden
[b] Lund Epilepsy Center, Department of Clinical Sciences, Lund University, Sweden
[c] Biomedical Imaging Unit, A.I. Virtanen Institute for Molecular Sciences, University of Eastern Finland, FIN-70 211, Kuopio, Finland
[d] Division of Neurology, Department of Clinical Sciences, Lund University, Sweden
[e] Ophthalmology, Department of Clinical Sciences Lund, Lund University, Sweden

ARTICLE INFO

*Keywords:*
Diffusion tensor imaging
Magnetic resonance imaging
Non-convulsive status epilepticus
Epilepsy
Retina
Inflammation

ABSTRACT

Pathophysiological consequences of focal non-convulsive status epilepticus (fNCSE) have been difficult to demonstrate in humans. In rats fNCSE pathology has been identified in the eyes. Here we evaluated the use of high-resolution 7 T structural $T_1$-weighted magnetic resonance imaging (MRI) and 9.4 T diffusion tensor imaging (DTI) for detecting hippocampal fNCSE-induced retinal pathology ex vivo in mice. Seven weeks post-fNCSE, increased number of $Iba1^+$ microglia were evident in the retina ipsilateral to the hemisphere with fNCSE, and morphologically more activated microglia were found in both ipsi- and contralateral retina compared to non-stimulated control mice. $T_1$-weighted intensity measurements of the contralateral retina showed a minor increase within the outer nuclear and plexiform layers of the lateral retina. $T_1$-weighted measurements were not performed in the ipsilateral retina due to technical difficulties. DTI fractional anisotropy(FA) values were discretely altered in the lateral part of the ipsilateral retina and unaltered in the contralateral retina. No changes were observed in the distal part of the optic nerve. The sensitivity of both imaging techniques for identifying larger retinal alteration was confirmed ex vivo in retinitis pigmentosa mice where a substantial neurodegeneration of the outer retinal layers is evident. With MR imaging a 50 % decrease in DTI FA values and significantly thinner retina in $T_1$-weighted images were detected. We conclude that retinal pathology after fNCSE in mice is subtle and present bilaterally. High-resolution $T_1$-weighted MRI and DTI independently did not detect the entire pathological retinal changes after fNCSE, but the combination of the two techniques indicated minor patchy structural changes.

## 1. Introduction

Epilepsy is a neurological disorder affecting over 50 million people worldwide. It manifests as epileptic seizures, i.e. spontaneous synchronized activity of neurons that disrupts the normal activity patterns in the brain. A prolonged epileptic seizure is called *status epilepticus* (SE) and it is categorized as focal or generalized SE depending on the extent of the abnormal activity (Holtkamp and Meierkord, 2011; Trinka

*Abbreviations:* CTRL, Control; DTI, Diffusion Tensor Imaging; EEG, electroencephalography; FA, Fractional Anisotropy; F-J, Fluoro-Jade; fNCSE, Focal Non Convulsive Status Epilepticus; GCL, Ganglion cell layer; GFAP, Glial fibrillary acidic protein; Iba1, Ionized calcium-binding adapter molecule 1; INL, Inner nuclear layer; IPL, Inner plexiform layer; KPBS, Potassium phosphate buffer saline; Map2, Microtubule-associated protein 2; MRI, Magnetic Resonance Imaging; OCT, optical coherence tomography; ONL, Outer nuclear layer; OPL, Outer plexiform layer; OS, Outer segments; PBS, Phosphate buffer saline; PFA, paraformaldehyde; rdKO, Retinal degeneration 1 $(Rd1)^{-/-}$ mice; ROI, Region of interest; SE, Status Epilepticus; WT, Wildtype.

* Corresponding author at: Inflammation and Stem Cell Therapy Group, Division of Clinical Neurophysiology, BMC A11, Sölvegatan 17, Lund University, SE-221 84, Lund, Sweden.
*E-mail address:* Christine.Ekdahl_Clementson@med.lu.se (C.T. Ekdahl).

https://doi.org/10.1016/j.eplepsyres.2021.106730
Received 16 April 2021; Received in revised form 30 June 2021; Accepted 16 July 2021
Available online 24 July 2021

et al., 2015; Walker, 2007).

The pathophysiological consequences of prolonged focal non-convulsive SE (fNCSE) have been difficult to visualise and predict with commonly used clinical imaging-techniques such as 3 T magnetic resonance imaging (MRI). Peri-ictal neuro-radiological findings are usually resolved within a month following fNCSE (Jabeen et al., 2017; Szabo et al., 2005). However, histological findings in rodents suggest distinct brain pathology following fNCSE, including neurodegeneration, gliosis and molecular changes (Avdic et al., 2018; Bonde et al., 2006; Brandt et al., 2003; Krsek et al., 2004; Vila Verde et al., 2021). In addition, it has been reported that rats with fNCSE in the temporal lobes also display pathological features in the retina in terms of activated glial cells and altered synaptic protein expression (Ahl et al., 2016). Hence, there is a need for complementary techniques that enable detection and prediction of retinal pathology that may follow fNCSE, as previously shown (Ahl et al., 2016).

In the present study, we evaluated the use of high-resolution 7 T structural $T_1$-weighted MRI and 9.4 T diffusion tensor imaging (DTI) techniques for detecting subtle fNCSE-induced retinal pathology in mice. The extent of retinal pathology post-fNCSE was evaluated with immunohistochemistry. In order to establish if prominent retinal damage is detectable with high-resolution MRI in a small structure such as the mouse retina, we used a genetic mouse model of retinitis pigmentosa, retinal degeneration 1 ($rd1^{-/-}$) mice, that presents with extensive neurodegeneration and gradual loss of photoreceptors in the retina (Faber et al., 1994; Semo et al., 2003).

## 2. Materials and methods

### 2.1. Animals and group assignment

All mice were housed in 12 h light-dark cycle with ad libitum food and water, and animal suffering was kept to a minimum according to the "Guide for care and use of laboratory animals" prepared by the National

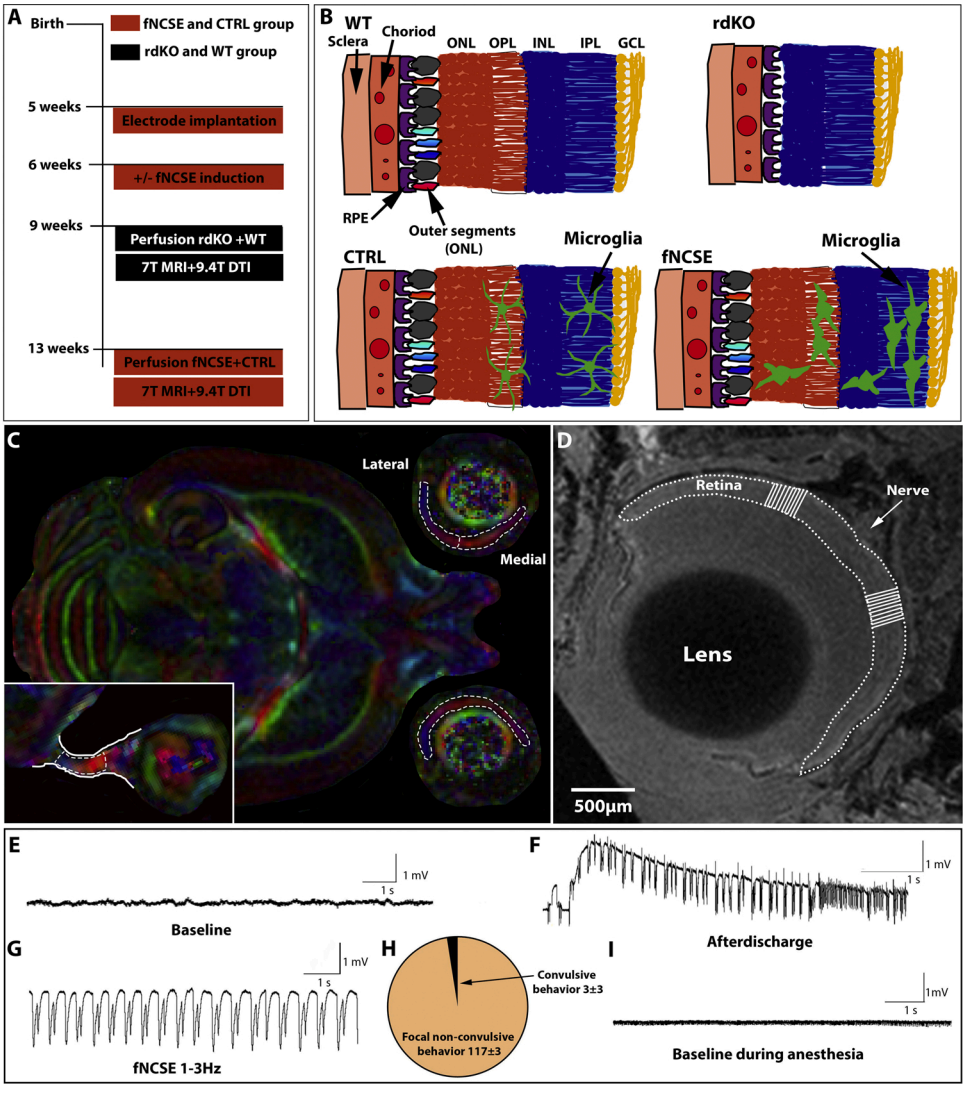


**Fig. 1.** (**A**) Timeline of the 2 different experimental groups. Controls (CTRL) and focal non-convulsive SE (fNCSE) mice were implanted with an electrode in the right hippocampus at the age of 5 weeks. One week later, animals were electrically induced with fNCSE, no stimulation was applied to CTRLs. Seven weeks after fNCSE induction, animals were perfused and imaged ex vivo. Retinal degeneration 1 $rd^{-/-}$ (rdKO) and wildtype (WT) animal were naïve when perfused at 13 weeks of age before ex vivo imaging. (**B**) Schematic drawing of the different structural layers in WT, rdKO, CTRL and fNCSE mice. In WT, overview from left to right: Sclera, choroid containing the vessels for the eye, retinal pigment epithelium (RPE), outer segments (OS) of the photoreceptors, outer nuclear layer (ONL) nucleus of the photoreceptors, outer plexiform layer (OPL), inner nuclear layer (INL), inner plexiform layer (IPL) the ganglion cell layer (GCL). The rdKO retina are at 2 months lacking both the ONL and OPL (upper right). The retina in CTRL and fNCSE animals have as the WT well defined retinal layers. The microglial distribution in CTLRs and during physiological conditions, are evenly spread in the plexiform layers with a ramified morphology. To the lower right, a schematic overview of previous findings in the rat retina: increased number of microglia with intermediate phenotype often in clusters, with migration to the nuclear layers (Ahl et al., 2016). (**C**) Representative FA-maps of brain and eyes. Voxels in FA maps of the entire retina was manually outlined and analysed (dotted lines) as well as region of interest in optic nerve (inset). (**D**) In $T_1$-weighted images, 10 adjacent lines were drawn through the entire retina (OS-GCL) on both the medial and lateral side of the contralateral eye. (*E*) EEG monitoring in the temporal lobe was conducted throughout the induction of fNCSE and background activity was registered in all fNCSE animals before electrical stimulation. (**F**) Individual after-discharge thresholds were then determined for all fNCSE animals before 1 h of supra-threshold electrical stimulation, leading to self-sustained continuous epileptiform activity typically with 1–3 Hz of spike/poly-spike-slow-wave activity (**G**). (**H**) During 2 h of continuous electrical epileptiform activity, the mice exhibited typical focal seizure semiology i.e. less consciousness, automatic and repetitive movements, and subtle motor signs, which occasionally evolved into bilateral convulsive behaviour (Racine, 1972). (**I**) Cessation of seizure activity with i.p. anaesthesia was confirmed with a supressed low voltage EEG background activity in all animals.

academy of sciences. All experimental procedures were approved by the regional Malmö/Lund committee for experimental animal use and the Swedish board of agriculture (permit number M93-14). Both male and female mice were included in the experiments (Fig. 1A). Two months old $Rd1^{-/-}$ mice (rdKO) with a $C_3H$ background, carrying a mutation in the gene encoding cGMP phosphodiesterase-6, (n = 4) were included to evaluate the use of the imaging techniques for detecting major structural changes in the retina. The rdKO mice exhibit substantial neurodegeneration and loss of photoreceptors. $C_3H$ strain- and age-matched wildtype mice (n = 4) were used as controls (WT). C57/bl mice, implanted with a unilateral electrode into the hippocampus, were divided into electrically induced fNCSE animals (n = 6) and non-stimulated, non-epileptic controls (CTRL) (n = 3) (Fig. 1**A-B**).

### 2.2. Electrode implantation and electrically induced focal non-convulsive status epilepticus

C57/bl mice (5 weeks old) were anaesthetized with 2 % isofluorane and implanted with a bipolar insulated stainless steel electrode (Plastics One, Roanoke, VA) into the right ventral CA1/CA3 region of the hippocampus (coordinates: 2.9 mm posterior and 3.0 mm lateral from bregma; and 3.0 mm ventral from dura, tooth bar set at −3.3 mm) for stimulation and electroencephalographic (EEG) recordings. A unipolar electrode was placed between the skull and adjacent muscle to serve as ground electrode. Following a week of recovery after surgery, mice were subjected to electrically-induced fNCSE according to previously described protocol (Avdic et al., 2018; Mohapel et al., 2004) (Fig. 1**E-I**). Electrode-implanted, non-stimulated strain and age-matched mice served as controls. Only mice that displayed self-sustained ictal EEG activity for 2 h in the temporal lobe with mainly partial seizure semiology according to Racine's scale (Racine, 1972), i.e. oro-facial twitches, nodding, drooling, and unilateral forelimb clonus, were included in this study. Behavioral symptoms and ictal EEG activity were completely interrupted after 2 h of self-sustained fNCSE by administration of pentobarbital (40 mg/kg, intraperitoneal injection).

### 2.3. Tissue preparation

Mice were deeply anaesthetised (9 weeks old rdKO mice or 7 weeks post-fNCSE, Fig. 1A) with intraperitoneal injection of pentobarbital (80 mg/kg) before perfusion with 0,9 % saline for 3 min and 4 % paraformaldehyde (PFA) in phosphate-buffer saline (PBS) for 15 min. Animals were subsequently decapitated and the entire heads were incubated in 4 % PFA for 24 h before shipment to Finland in potassium PBS (KPBS) for *ex-vivo* MRI.

### 2.4. 9.4 T DTI and data processing

After perfusion, mice brains and both eyes were imaged *ex vivo* in a 9.4 T magnet (Oxford Instruments PLC, Abingdon, UK). Diffusion data was acquired using a spin-echo-echo-planar-imaging sequence using a TR/TE = 1000/35 ms, echo spacing =0.664 ms, number of shots = 6, bandwidth = 250000 Hz, number of averages = 1, FOV = 16 × 16.5 × 18 $mm^3$, spatial resolution = 125 × 125 × 125 $\mu m^3$, number of diffusion directions = 42, b-value = 3039.6 $s/mm^2$, number of minimally diffusion weighted images = 1, gradient amplitude = 35.11 G/cm, gradient duration (δ)/separation (δ) = 6/11.50 ms, acquisition time =10 h 48 min. Data was processed with in-house codes using Matlab (ver. R2012b, MathWorks, Natick, Massachusetts, U.S.A.) to reconstruct diffusion weighted images. Each diffusion weighted dataset was corrected for residual eddy current induced geometric distortions using the relevant toolbox in Explore DTI (Leemans and Jones, 2009)(www.exploredti.com). In order to increase anatomical contrast, diffusion weighted data was sampled by a factor of two using B-spline interpolation, and a voxel-wise fit of the diffusion tensor model was performed to generate fractional anisotropy (FA) maps.

### 2.5. 7 T $T_1$ MRI

Due to disturbances of the cavity left by the electrode in the hippocampus on the ipsilateral side, only the contralateral eye was imaged using a single loop coil in a horizontal bore 7 T-magnet (Bruker Pharmascan). 3D $T_1$W-FLASH (GE without fluid attenuation) data were acquired using a TR/TE = 150/7.2 ms, number of averages = 4, FOV = 1.17 × 1.17 × 1.17 $mm^3$, spatial resolution = 26 × 26 × 26 $\mu m^3$, and acquisition time =12 h 32 min.

### 2.6. Imaging analysis and intensity measurements of mice eyes ex vivo

#### 2.6.1. Analysis of FA maps

DTI provides information of the tissue at a microstructural level. DTI is sensitive to the movement of water molecules within the tissue, which reflects tissue microstructure. FA related to organization of the microstructure and orientation are information extracted from DTI. Analyses of FA maps were done in an in-house tool, Aedes, built in MATLAB software (https://github.com/mjnissi/aedes). The entire retina was manually outlined in 8 adjacent slices, from the most central parts of the eye, resulting in a region of interest (ROI) (Fig. 1C) where the mean FA of the entire retina was measured, and the percentage of voxels below the threshold of 0.1 was estimated (**Supplementary Fig. 1**). The retina in FA maps in the fNCSE group appeared more heterogeneous, and in an attempt to investigate if the low FA values in the fNCSE animals were consistent with the pathology, an additional analysis separating the medial and lateral parts of the retina was performed. In addition, the mean FA values of the optic nerve (Fig. 1C, inset) were analysed and voxels were manually outlined in the distal part of the optic nerve close to the eye, in 5 adjacent sections. The left and right retina in rdKO and WT animals were homogenous in terms of pathology, hence, only the left eye was included in the analysis. Since brain pathology following fNCSE was more prominent ipsilaterally, both ipsi- (right) and contra- lateral (left) eyes were included in the analysis of fNCSE and CTRL group.

### 2.7. Analysis of $T_1$ 7 T images

For the analysis of the $T_1$-weighed images, software ImageJ with built-in functions was used. To standardize the intensity in the $T_1$ images, all values were normalized to the individuals lens intensity. For each eye, 10 lines were drawn emanating from the most central part of the eye - where the nerve fuses with the retina - from the choroid through all layers of the retina, i.e. from the outer part of outer nuclear layer (ONL) to the inner part of ganglion cell layer (GCL) on both the lateral and medial side of the contralateral eye (Fig. 1D). Each line represented the individual mean intensity value of all the retinal layers outer segments (OS), ONL, outer plexiform layer (OPL), inner nuclear layer (INL), inner plexiform layer (IPL), and GCL. For visual representation a heatmap (from 0−338 μm) depicting the mean intensity of all 10 lines for each animal is presented. Furthermore, since our earlier studies have reported a change in microglial number and morphology mainly in the plexiform layers, the intensity of the retina was also divided into outer retinal layers OS, ONL, and OPL and inner INL, IPL and GCL to create some margin to ensure the plexiform layers were included separately. This enabled the investigation of more regional alterations in MRI intensity in the OPL and IPL retinal layers respectively. The intensity of the optical nerve was measured in an area of approximately 25–30 $\mu m^2$ in 5–10 adjacent sections in fNCSE and rdKO mice, and their respective controls.

### 2.8. Immunohistochemistry and Fluoro-Jade staining of the mice retina

After MRI acquisition, the extent of retinal pathology was evaluated with immunohistochemical stainings. The eyes were removed from the skull and incubated in 10 % sucrose for 16 h and 20 % sucrose for 24 h before imbedded in Yazulla medium (30 % egg albumin, 3 % gelatin).

Eyes were cut into 20 μm thick slices using a cryostat (Microm HM 560, USA) and sections were stored at -20 °C until use. Eye sections were rinsed in PBS before blocking in 5 % serum for 1.5 h. Sections were incubated in primary antibody at 4 °C overnight. Primary antibodies used were rabbit anti-mouse Iba1 (1:500 Wako, Japan), mouse anti-mouse Glial Fibrillary Acidic Protein (GFAP) (1:500 Sigma Aldrich), rabbit anti-mouse microtubule-associated protein (Map2) (1:200 Cell Signaling, USA). The following day, slides were washed before incubated with secondary antibody for 2 h in room temperature. Secondary antibodies used were Cy3-donkey anti-rabbit, Cy3-goat anti-mouse and Alexa-488 donkey anti-rabbit (1:200 Jackson ImmunoResearch, USA). Lastly, sections were washed and cover-slipped with DABCO (Merck, Germany) containing 1:1000 Hoescht (Thermofisher).

For Fluoro-Jade (F-J) staining, sections were washed with KPBS, hydrated and pre-treated with 0.06 % potassium permanganate for 15 min, rinsed with distilled water and treated with 0.001 % F-J (Histo-Chem, Jefferson, AR, USA) for 30 min. They were then washed with distilled water, dehydrated with ethanol and xylene, and finally cover-slipped with Pertex mounting medium (Histolab, Sweden).

### 2.9. Morphological analyses and cell counting in Iba1, GFAP, Map2 and Flouro-Jade staining

The retina consists of several highly specialized and well-defined layers: OS, ONL, OPL, INL, IPL, GCL) (Fig. 1**B**). The Iba1 staining was evaluated in 12 retinal sections of the left and right eye, respectively, where the number of cells was quantified specifically in 2 regions of interest (approximately 27 000 $\mu m^2$) per section, using an Olympus BX61 epifluorescence microscope (Leica, Germany). In the CTRLs and fNCSE animals, where all retinal layers were present, cells in IPL and OPL were quantified separately. Since the rdKO mice lack the outer retinal layers, microglial analysis was only performed in IPL of these mice and the corresponding control (WT) mice. Data are presented as the number of $Iba1^+$ cells/ROI. For morphological analysis, a total of 120 $Iba1^+$ cells were analyzed per retina for three different activity stages of microglia, i.e. ramified (resting microglia with small cell soma and long processes), intermediate (activated microglia with bigger, elongated cell soma and fewer and thicker processes) and round/amoeboid (fully activated phagocytic microglia characterized by large cell soma with little processes). The relative occurrence of each subtype of microglia is expressed as the mean percentage of $Iba1^+$ cells per retina. The GFAP expression in Müller cell end-feet in GCL was evaluated in pictures acquired using epifluorescence microscope (Olympus BX61) and the mean GFAP intensity from 5 different sections of the GCL were measured using ImageJ. The analysis included 12 images of the left and right retina, respectively. The rdKOs displayed an additional phenomenon with GFAP upregulation in Müller cell processes extending into the IPL. This was not observed in either fNCSE or CTRL mice. Therefore, the GFAP expression in Müller cell processes was graded and evaluated together with their length and thickness in rdKOs and WTs only (for details on evaluation see **Supplementary Table 1**). In addition, the gross morphology of neurons in the retina was evaluated by analyzing Map2, a microtubule-associated protein, shown to be highly expressed in the GCL (Okabe et al., 1989). In the healthy retina, the GCL is generally one ganglion cell layer thick, and although cells are packed closely together, they are separated by glial Müller processes.

In order to evaluate the organization of processes and cell bodies expressing Map2 in the GCL, the number of interruptions was defined as the number of dark patched areas in the GCL, lacking Map2 expression. In addition, Map2 intensity was measured in all groups in 6–8 pictures per animal/retina using an epifluorescence microscope. With ImageJ the mean intensities of the GCL and IPL areas were measured in the ipsi- and contralateral retina, respectively. To evaluate the number of apoptotic cells, $F\text{-}J^+$ cells were quantified in the entire retina in 4 sections per eye, in both eyes, in all 4 groups (CTRL, fNCSE, rdKO and WT). Due to poor tissue condition, n = 2 fNCSE animals had to be excluded from histological quantifications.

### 2.10. Statistics

For all cell quantifications and intensity measurements, $T_1$ MRI and DTI evaluations that showed normal distribution according to Shapiro Wilks test, a parametric unpaired *t*-test was used for comparison of 2 groups. The grading of GFAP expression in Müller cells and GFAP intensity in rdKO and WT, which showed a scattered distribution of values, were compared with non-parametric Mann-Whitney test. For evaluation of microglial morphology and the heatmaps of $T_1$-weighted intensities, a 2-way ANOVA with Bonferroni correction was applied. Parametric data are presented as mean ± standard error of mean, and non-parametric data are presented as median + interquartile range. All p-values $<0.05$ were considered statistically significant.

## 3. Results

### 3.1. Activation of microglia in the retina after focal non-convulsive status epilepticus and in rdKO mice

As expected, rdKO mice displayed prominent cell death, structural differences and neuronal degeneration in the outer layers of the retina, which only enabled quantification of $Iba1^+$ cells in the IPL (Fig. 2**A**) where increased numbers were found in rdKO compared WT mice ($p = 0.0002$) (Fig. 2**B**). Microglial morphology showed a modest, but significant interaction ($p = 0.02$) with a decrease in ramified morphology in the rdKO mice (Fig. 2**B**). Analysis of $Iba1^+$ cell numbers in the fNCSE group revealed a significant increase in both IPL and OPL in the ipsilateral retina (Fig. 2**C**) ($p_{ipsiIPL} = 0.006$, $p_{ipsiOPL} = 0.03$), but no changes in the contralateral retina ($p_{contraIPL} = 0.14$, $p_{contraOPL} = 0.57$). Morphological evaluation showed a decrease in ramified and an increase in intermediate phenotype bilaterally ($p_{ipsi} = 0.001$, $p_{contra} = 0.006$) (Fig. 2**A**, **C**).

Analysis of GFAP intensity was performed in the GCL where glial cells including astrocytes and Müller cells are present. GFAP intensity in the GCL did not differ in either rdKO mice **(Figure D, E)** or fNCSE mice (Fig. 2**D, F**) compared to their respective control groups ($p_{rdKOvsWT} = 0.06$, $p_{fNCSEvsCTRL} = 0.42$ (ipsi), 0.79 (contra)). $GFAP^+$ Müller cell processes that extend out to the OPL were evident in the rdKO mice (Fig. 2**D**, **arrow**) with a significant upregulation of GFAP compared to WT mice ($p_{No.} = 0.03$, $p_{lenght} = 0.03$, $p_{thickness} = 0.03$) (Fig. 2**E**). Though this phenomenon has previously also been demonstrated following fNCSE in rats (Ahl et al., 2016), it was absent in the fNCSE mice (Fig. 2**D**).

### 3.2. Neuronal death in retina of rdKO mice while preserved neuronal structures following focal non-convulsive status epilepticus

In WT mice, Map2 staining appeared homogenous in all layers, whereas substantial disruption of retinal cell layers, including the OPL, was evident in rdKO mice (Fig. 2G). RdKO mice also displayed a substantial loss of retinal ganglion cells and a disseminated integrity of the GCL (Fig. 2**G, H**), though Map2 intensity analysis of GCL did not show differences compared to WT mice (GCL: $p = 0.15$ WT = 30 ± 2.7 vs rdKO = 35 ± 2.0, IPL: $p = 0.59$ WT = 38 ± 4.3 vs rdKO = 41 ± 3.5). In fNCSE mice, the distribution of Map2 appeared homogenous and there was no difference in number of GCL interruptions compared to CTRLs (Fig. 2**G**, **I**), and no change in Map2 intensity in the GCL and IPL (GCL: ipsi $p = 0.41$ CTRL 34 ± 0.8 vs fNCSE 38 ± 3.4, contra $p = 0.99$ CTRL 35 ± 3.5 vs fNCSE 35 ± 2.8, IPL: ipsi $p = 0.87$ CTRL 43 ± 2.7 vs fNCSE 44 ± 3.6, contra $p = 0.36$ CTRL 46 ± 4.8 vs fNCSE 40 ± 2.1).

The total number of $F\text{-}J^+$ cells was significantly increased in rdKOs compared to WT (Fig. 2**J**, **K**) ($p = 0.04$). No differences in numbers of $F\text{-}J^+$ cells were observed between fNCSE and CTRLs (Fig. 2**J**, **L**) ($p_{ipsi} = 0.64$, $p_{contra} = 0.26$).

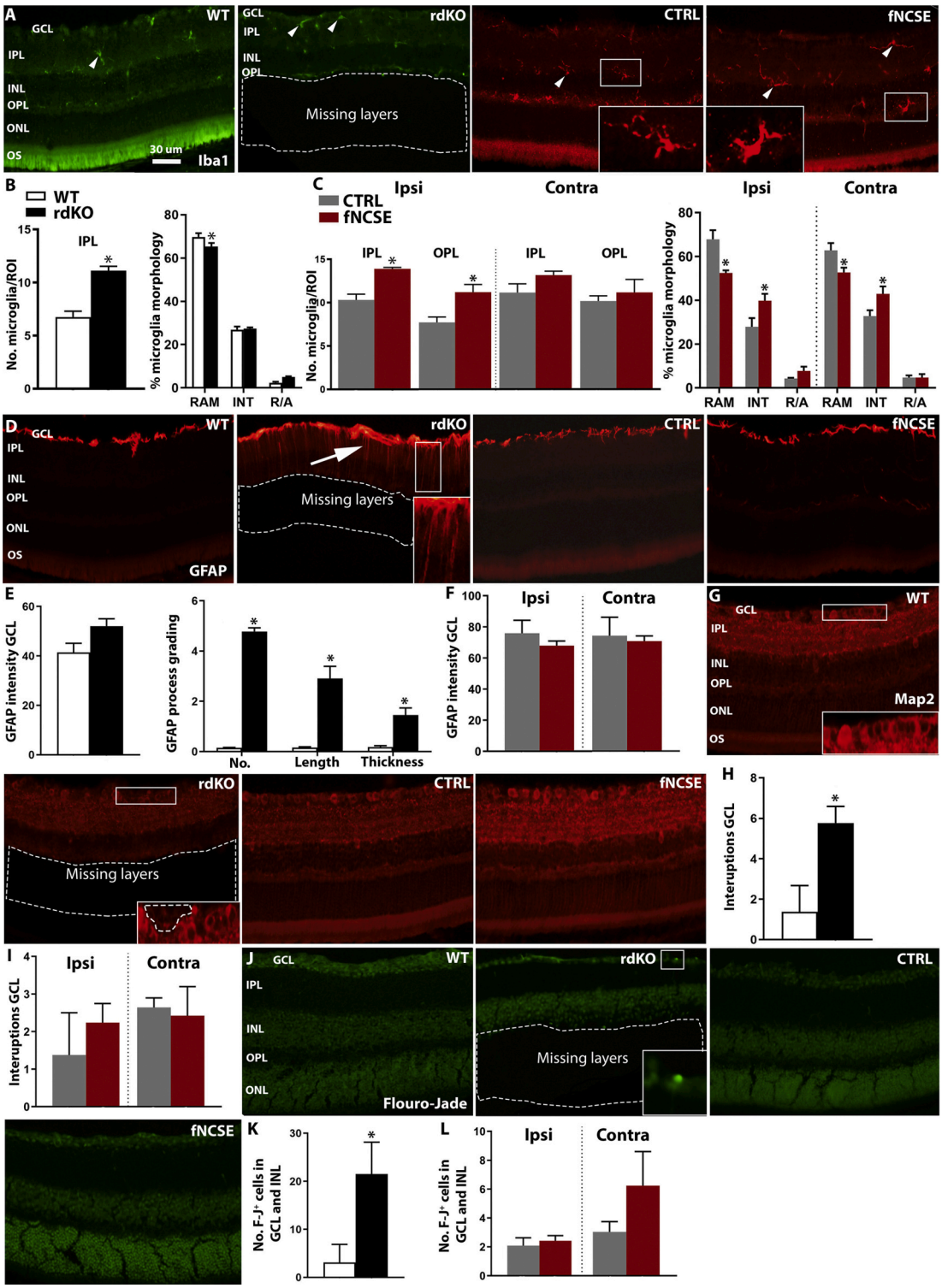


**Fig. 2.** Panel (**A**) Representative images of immunohistochemical Iba1$^+$ cells (microglia) staining in WT, rdKO, CTRL and fNCSE mice. Inset in CTRL represents ramified, and the inset in fNCSE displays intermediate microglia. (**B**) The rdKOs were as expected missing the outer retinal layers. They displayed a higher number of Iba1$^+$ cells (arrow heads) and altered Iba1 morphology with decreased number of ramified cells. (**C**) The fNCSE animals had higher numbers of Iba1$^+$ cells in IPL and OPL in the ipsilateral eye. The morphology was changed in both the ipsi- and contralateral retina, displaying more intermediate and less ramified phenotype. Panel (**D**) display representative images of the GFAP staining. Arrow and inset show increased GFAP expression in the Müller cell processes in rdKO, not in fNCSE mice. (**E**) In the rdKO, no alteration in GFAP intensity in the GCL was found, but increased number (No.), length and thickness of the GFAP positive Müller cell processes compared to WT. (**F**) No changes in GFAP intensity in GCL in fNCSE compared to CTRL mice. Panel (**G**) presents Map2 staining of neuronal network in WT, rdKO, CTRL and fNCSE mice. The marked area in the rdKO inset displays interruptions of GCL, significantly increased in the rdKO mice (**H**). (**I**) No changes of GCL interruptions were found in the fNCSE mice. (J) Representative Fluoro-Jade (FJ) staining in WT, rdKO, CTRL and fNCSE mice. Inset in rdKO shows F-J$^+$ degenerating neuron. (**K**) Increased numbers of F-J$^+$ cells in rdKO animals compared to WT, while no difference were observed between fNCSE and CTRL mice (**L**). All graphs are presented as mean + standard error of mean, except for the GFAP data in the rdKO and WT which is presented as median with the inner quartile range, since it was not normally distributed. *p $>$ 0.05. $n_{WT} = 4$ vs $n_{Rd1} = 4$ and $n_{CTR} = 3$ vs $n_{fNCSE} = 3$.

### 3.3. Discrete heterogeneity in FA maps of the mouse retina after focal non-convulsive status epilepticus

The rdKO retina appeared overall thinner and darker compared to the WT group (Fig. 3A, **B**). Consistently, FA values in the rdKO retina were significantly lower compared to the WT animals (Fig. 3**C**), while no changes were observed in the distal part of the optic nerve (Fig. 3**C**). FA values of the entire retina in fNCSE were unaltered in both the ipsi- and contralateral eye (Fig. 3**D-G**) and the optic nerve ($p_{ipsi} = 0.34$, $p_{conta} = 0.06$) compared to CTRLs (Fig. 3G). Neither did the percentage of voxels with FA values <0.1 differ between fNCSE and CTRL animals ($p = 0.55$, CTRL 43 ± 3 % vs fNCSE 46 ± 4 %). When sub-dividing the retina into lateral and medial part, the FA values were significant decreased in the lateral part of the ipsilateral retina ($p_{lateral} = 0.02$, $p_{medial} = 0.21$) (Fig. 3**H**), which is mostly innervated by the ipsilateral brain hemisphere with the electrode, and epileptic focus. No differences were found in FA values in the lateral or medial part of the contralateral retina ($p_{lateral} = 0.87$, $p_{medial} = 0.88$) (Fig. 3**I**).

### 3.4. Minor changes in $T_1$-weighted retinal images after focal non-convulsive status epilepticus

Visual analysis of $T_1$-weighted images suggested a thinner and darker retina in rdKO compared to WT mice (Fig. 4A) and the vitreous body, known to be altered in numerous diseases (Monteiro et al., 2015), also displayed a darker colour. Statistical analysis revealed a lower vitreous intensity in rdKO animals compared to WT (mean grey value normalized to lens intensity WT 5.4 ± 0.15 vs rdKO 4.5 ± 0.14, $p = 0.01$). Intensity measurements of the distal optic nerve showed no differences between groups (WT 6.1 ± 0.23 vs rdKO 5.6 ± 0.18). Analysis of the heatmaps representing the $T_1$ intensity through the different retinal layers displayed a thinner retina in rdKOs (156 µm in all mice) compared with WTs (312−338 µm), though, no significant alterations in intensity could be found within the 156 µm of either lateral or medial retina in rdKOs compared to WTs (Fig. 4**B**, **C**).

In the fNCSE and CTRL mice, no significant differences were detected in the choroid mean intensity (contralateral eye: medial part CTRL = 7.7 ± 0.62 vs fNCSE 8.8 ± 0.24, $p = 0.09$; lateral part CTRL 7.5 ± 0.54 vs fNCSE 7.8 ± 0.31, $p = 0.07$). Analysis of the heatmaps (286−312 µm) showed no differences in lateral or medial part of the contralateral retina, but when subdividing the retinal layers into outer (ONL + OPL) and inner layers (INL + IPL) fNSCE mice exhibited a minor increase in the $T_1$ intensity at position 0 and 130 µm of the lateral retina compared to CTRL ($p_{lateral} = 0.004$, $p_{medial} = 0.22$) (Fig. 4**D-H**). No intensity changes in the optic nerve were observed in fNCSE compared to CTRL mice (contralateral nerve CTRL: 5.9 ± 0.41 vs fNCSE 5.5 ± 0.28, $p = 0.08$). No measurements were performed on the ipsilateral retina.

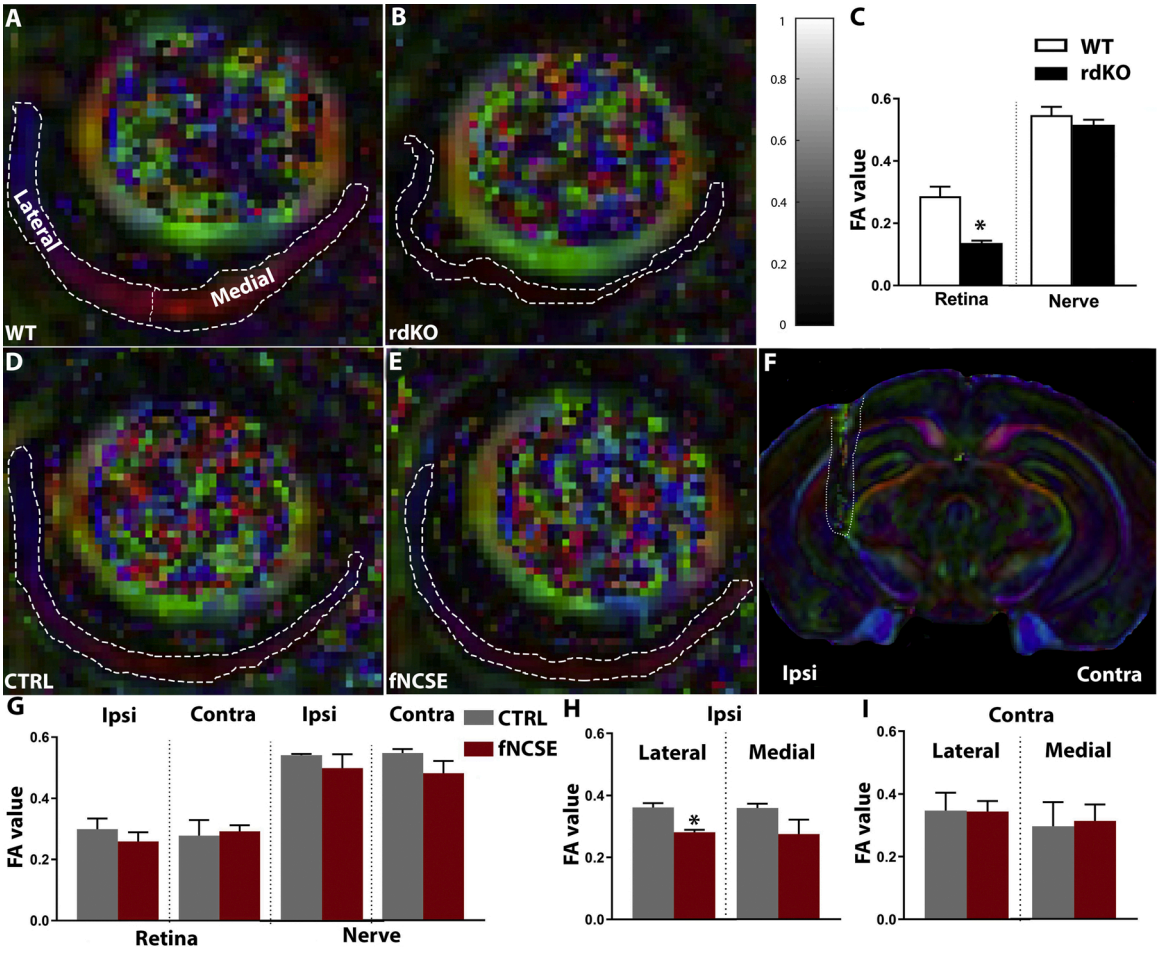


**Fig. 3.** Representative sections of colour coded FA maps in WT (**A**) and rdKO with a greyscale bar of FA values (**B**). (**C**) Mean FA values in rdKO retina were significantly lower compared to WT without changes in the optic nerve. Representative sections of CTRL (**D**) and fNCSE (**E**) that on occasion displayed darker patches. (**F**) Cavity from an electrode in the brain in a dorsal-ventral direction. (**G**) fNCSE showed no differences in non-colour FA-values in the retina or the optical nerve compared to CTRL. (**H, I**) When dividing the retina into medial and lateral parts, a significant decrease in FA values in the ipsilateral retina on the lateral side was observed. *$p > 0.05$. $n_{WT} = 4$ vs $n_{Rd1} = 4$ and $n_{CTR} = 3$ vs $n_{fNCSE} = 5$.

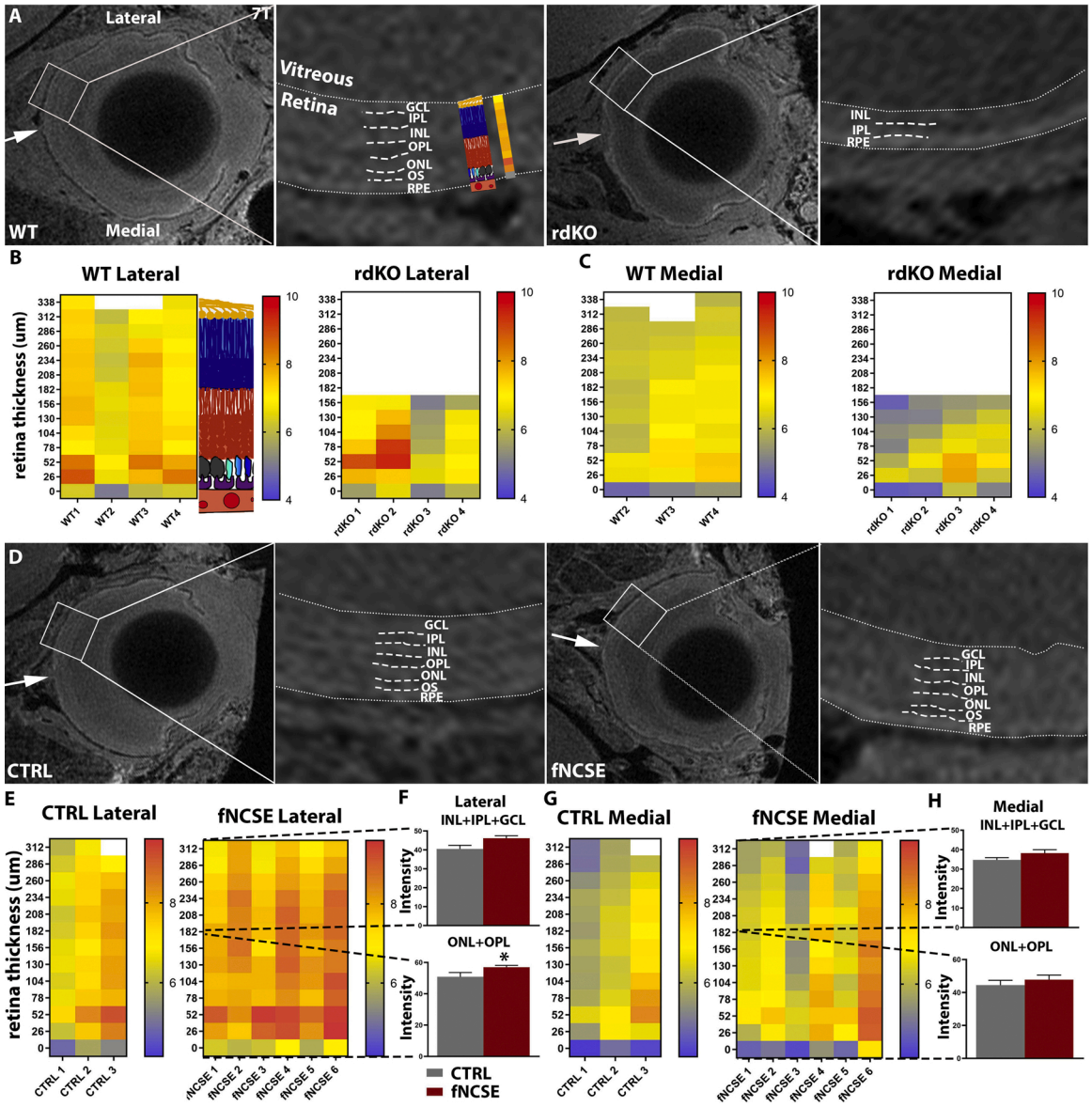


**Fig. 4.** Panel (**A**), represents $T_1$-weighted images of WT and rdKO eyes. Arrows indicate the placement of the optic nerve. To the right a magnification of the retina (see dotted lines) and a display of the retinal layers. For clarification of retinal layering see schematic and heatmap inset. (**B**, **C**) Heatmaps represent mean intensity of 10 lines from position 0−338 μm (Y-axis), for each animal (X-axis). The heatmaps of rdKO mice were shorter than WT maps on both the lateral and medial side, reflecting rdKOs pervading pathology. No difference in intensity was found in the remaining rdKOs retinal layers (INL, IPL and RPE) from position 0–156 μm compared to WT. In panel (**D**), representative T1-weighted images of the contralateral eye of CTRL and fNCSE. Visually fNCSE mice exhibited similar retinal layering as CTRLs, apart from occasional heterogenous areas where the retinal layers were harder to distinguish. (**E-H**) Statistical analysis of the heatmap on the lateral and medial side of the retina, subdividing the retina into outer and inner retinal layers, identified a significant increase in $T_1$ intensity on retinal position 0–182 μm (ONL + OPL) in the lateral retina in fNCSE animals compared to CTRLs. *$p > 0.05$. $n_{WT} = 4$ vs $n_{Rd1} = 4$ and $n_{CTR} = 3$ vs $n_{fNCSE} = 6$.

## 4. Discussion

In this study, we evaluated the use of high-resolution structural MRI techniques for detecting subtle fNCSE-induced retinal pathology in mice. Additionally, mice with retinitis pigmentosa, known to have retinal neurodegeneration and inflammation, were included as positive controls for extensive retinal pathology. Both imaging techniques, 7 T $T_1$-weighted and 9.4 T DTI, proved to be sensitive enough for detecting prominent retinal layer distortions in the mouse model of retinitis pigmentosa. DTI FA values decreased with 50 % in the retina and a thinner retina was confirmed with MRI $T_1$-weighted images in rdKO compared to WT mice. In mice with fNCSE, histopathological analysis revealed bilateral microglial activation; more in the ipsi- compared to contralateral retina. FA values were discretely altered in the lateral part of the ipsilateral retina, and $T_1$-weighted intensity changed in the outer layers of the lateral part of the contralateral retina.

Our earlier study in rats revealed prominent micro- and macro-glial responses, changes in synaptic protein expression and alterations in cytokine and chemokine levels in the retina bilaterally post-fNCSE. In the present study with the same fNCSE induction in mice, a similar pathological profile was present, but not as pronounced. Activated microglia were distributed randomly and mainly in the plexiform layers in both the ipsi- and contralateral retina, indicating changes in their normal function as regulators of synaptic transmission (Paolicelli et al., 2011; Roumier et al., 2004), although not appearing in clusters as previously observed in rats (Ahl et al., 2016). The discrepancies may be attributed to differences in e.g. the immune system or cerebrovascular anatomy between animals and rodent strains (Barone et al., 1993;

Becker, 2016; Prieto et al., 2005) or that the propagation of epileptic activity per se may differ (Boswell et al., 2014). In addition, we did not discriminate between the lateral and medial part of the retina in the immunohistochemical analysis. If the immune reaction is more pronounced on one side of the retina, medial or lateral, related to the unilaterally generated fNCSE, sub-retinal alterations relevant to epileptic activity confined to certain parts of the brain may have been overlooked.

The FA maps showed minor retinal irregularities in mice with fNCSE; a discrete observation in the lateral part of the ipsilateral eye. Whether or not this unilateral retinal manifestation may be related to the fNCSE originating in the ipsilateral brain hemisphere is unclear. Conversely, the $T_1$-weighted images indicated minor alterations in the OPL on the lateral side of the contralateral retina. This is not the part of the retina primarily innervated by the hemisphere with fNCSE and whether it is related to propagated bilateral seizure activity or lack pathological significance is unknown.

High-resolution MRI has emerged in clinical practice, providing enhanced resolution and better clinical outcomes (Trattnig et al., 2018). Although it offers unique advantages when studying the CNS non-invasively, there are limitations to be considered when evaluating its use for detecting fNCSE retinal pathology. First, we encountered technical difficulties in the $T_1$-weighted images, since artefacts from the electrode cavity within the temporal lobe prevented a successful imaging of the ipsilateral eye. Since the fNCSE mice displays primarily unilateral damage, the ipsilateral eye would have added further value to this matter. Second, imaging a small structure such as the mouse retina and its discrete pathology within certain retinal layers challenges the detection range. The present $T_1$-weighted images with a resolution of 26 μm were not sensitive enough to convincingly define the entire histological changes in the contralateral retina. Third, while DTI might offer more specificity when detecting microstructural changes, the lower resolution of 125 μm was too limited for consistently defining the bilateral immune reaction in the retinal structures after fNCSE.

Other imaging modalities such as optical coherence tomography (OCT) may be more feasible methods to use for detecting discrete retinal changes in neurological diseases, as previously described in Parkinson's disease, Alzheimer's disease and multiple sclerosis (Jindahra et al., 2010; Kim et al., 2009; Sakamoto et al., 2010). In a recent OCT study, thinner retinal nerve fiber layer, GCL, and IPL were identified in patients with epilepsy, suggesting retinal neurodegeneration. The authors also observed thickening of the choroid indicating changes in retinal vascularization and neuroinflammation (Tak et al., 2019). Indeed, changes in retinal vascularization might be another aspect and an attractive target for visualizing retinal impairment in the context of fNCSE-induced pathology. Again, these observations warrant further evaluation in order to define the retinal pathology and stratify the potential of retinal imaging as a diagnostic and prognostic biomarker in epilepsy.

## 5. Conclusion

After fNCSE in mice, an immune response was observed in both the ipsi- and contralateral retina. Due to limitations in $T_1$ specificity and the lower resolution with DTI, the entire bilateral immune reaction in the retina following fNCSE in mice was not convincingly identified. However, the combination of the two imaging techniques indicated subtle patchy structural alterations. Prominent retinal pathology such as reorganization of layers in retinitis pigmentosa mice (rd1KO) was detected with high-resolution MRI, both $T_1$-weighted imaging and DTI acquisition.

## Acknowledgements and funding

We kindly thank Assoc Prof Per Eklund, LU, for providing us with the rdKO animals in this study. We are also thankful to Michael Ljungholm and Karin Markenroth-Bloch, LU, for their valuable input regarding the MRI/DTI results. This research has received financial support from ALF, Swedish Research Council, Epitarget – a European Union's Seventh Framework Programme (FP7/2007-2013) under grant agreement no. 602102, Fund for visually disabled in Southern Sweden, and Crown Princess Margareta's Fund for visually disabled. Alejandra Sierra thanks Academy of Finland for their financial support.

## Appendix A. Supplementary data

Supplementary material related to this article can be found, in the online version, at doi:https://doi.org/10.1016/j.eplepsyres.2021.106730.

## References

Ahl, M., Avdic, U., Skoug, C., Ali, I., Chugh, D., Johansson, U.E., Ekdahl, C.T., 2016. Immune response in the eye following epileptic seizures. J. Neuroinflammation 13, 155.
Avdic, U., Ahl, M., Chugh, D., Ali, I., Chary, K., Sierra, A., Ekdahl, C.T., 2018. Nonconvulsive status epilepticus in rats leads to brain pathology. Epilepsia 59, 945–958.
Barone, F.C., Knudsen, D.J., Nelson, A.H., Feuerstein, G.Z., Willette, R.N., 1993. Mouse strain differences in susceptibility to cerebral ischemia are related to cerebral vascular anatomy. J. Cereb. Blood Flow Metab. 13, 683–692.
Becker, K.J., 2016. Strain-related differences in the immune response: relevance to human stroke. Transl. Stroke Res. 7, 303–312.
Bonde, S., Ekdahl, C.T., Lindvall, O., 2006. Long-term neuronal replacement in adult rat hippocampus after status epilepticus despite chronic inflammation. Eur. J. Neurosci. 23, 965–974.
Boswell, C.A., Mundo, E.E., Ulufatu, S., Bumbaca, D., Cahaya, H.S., Majidy, N., Van Hoy, M., Schweiger, M.G., Fielder, P.J., Prabhu, S., Khawli, L.A., 2014. Comparative physiology of mice and rats: radiometric measurement of vascular parameters in rodent tissues. Mol. Pharm. 11, 1591–1598.
Brandt, C., Glien, M., Potschka, H., Volk, H., Löscher, W., 2003. Epileptogenesis and neuropathology after different types of status epilepticus induced by prolonged electrical stimulation of the basolateral amygdala in rats. Epilepsy Res. 55, 83–103.
Faber, D.B., F.J, Bowes-Rickman, C., 1994. The rd mouse story: seventy years of research on an animal model of inherited retinal degeneration. Prog. Retin. Eye Res. 13, 31–64.
Holtkamp, M., Meierkord, H., 2011. Nonconvulsive status epilepticus: a diagnostic and therapeutic challenge in the intensive care setting. Ther. Adv. Neurol. Disord. 4, 169–181.
Jabeen, S.A., Cherukuri, P., Mridula, R., Harshavardhana, K.R., Gaddamanugu, P., Sarva, S., Meena, A.K., Borgohain, R., Jyotsna Rani, Y., 2017. A prospective study of diffusion weighted magnetic resonance imaging abnormalities in patients with cluster of seizures and status epilepticus. Clin. Neurol. Neurosurg. 155, 70–74.
Jindahra, P., Hedges, T.R., Mendoza-Santiesteban, C.E., Plant, G.T., 2010. Optical coherence tomography of the retina: applications in neurology. Curr. Opin. Neurol. 23, 16–23.
Kim, J.S., Ishikawa, H., Sung, K.R., Xu, J., Wollstein, G., Bilonick, R.A., Gabriele, M.L., Kagemann, L., Duker, J.S., Fujimoto, J.G., Schuman, J.S., 2009. Retinal nerve fibre layer thickness measurement reproducibility improved with spectral domain optical coherence tomography. Br. J. Ophthalmol. 93, 1057–1063.
Krsek, P., Mikulecká, A., Druga, R., Kubová, H., Hlinák, Z., Suchomelová, L., Mares, P., 2004. Long-term behavioral and morphological consequences of nonconvulsive status epilepticus in rats. Epilepsy Behav. 5, 180–191.
Leemans, A., Jones, D.K., 2009. The B-matrix must be rotated when correcting for subject motion in DTI data. Magn. Reson. Med. 61, 1336–1349.
Mohapel, P., Ekdahl, C.T., Lindvall, O., 2004. Status epilepticus severity influences the long-term outcome of neurogenesis in the adult dentate gyrus. Neurobiol. Dis. 15, 196–205.
Monteiro, J.P., Santos, F.M., Rocha, A.S., Castro-de-Sousa, J.P., Queiroz, J.A., Passarinha, L.A., Tomaz, C.T., 2015. Vitreous humor in the pathologic scope: insights from proteomic approaches. Proteomics Clin. Appl. 9, 187–202.
Okabe, S., Shiomura, Y., Hirokawa, N., 1989. Immunocytochemical localization of microtubule-associated proteins 1A and 2 in the rat retina. Brain Res. 483, 335–346.
Paolicelli, R.C., Bolasco, G., Pagani, F., Maggi, L., Scianni, M., Panzanelli, P., Giustetto, M., Ferreira, T.A., Guiducci, E., Dumas, L., Ragozzino, D., Gross, C.T., 2011. Synaptic pruning by microglia is necessary for normal brain development. Science (New York, N.Y.) 333, 1456–1458.
Prieto, R., Carceller, F., Roda, J.M., Avendano, C., 2005. The intraluminal thread model revisited: rat strain differences in local cerebral blood flow. Neurol. Res. 27, 47–52.
Racine, R.J., 1972. Modification of seizure activity by electrical stimulation. II. Motor seizure. Electroencephalogr. Clin. Neurophysiol. 32, 281–294.
Roumier, A., Bechade, C., Poncer, J.C., Smalla, K.H., Tomasello, E., Vivier, E., Gundelfinger, E.D., Triller, A., Bessis, A., 2004. Impaired synaptic function in the microglial KARAP/DAP12-deficient mouse. J. Neurosci. 24, 11421–11428.
Sakamoto, A., Hangai, M., Nukada, M., Nakanishi, H., Mori, S., Kotera, Y., Inoue, R., Yoshimura, N., 2010. Three-dimensional imaging of the macular retinal nerve fiber

layer in glaucoma with spectral-domain optical coherence tomography. Invest. Ophthalmol. Vis. Sci. 51, 5062–5070.
Semo, M., Peirson, S., Lupi, D., Lucas, R.J., Jeffery, G., Foster, R.G., 2003. Melanopsin retinal ganglion cells and the maintenance of circadian and pupillary responses to light in aged rodless/coneless (rd/rd cl) mice. Eur. J. Neurosci. 17, 1793–1801.
Szabo, K., Poepel, A., Pohlmann-Eden, B., Hirsch, J., Back, T., Sedlaczek, O., Hennerici, M., Gass, A., 2005. Diffusion-weighted and perfusion MRI demonstrates parenchymal changes in complex partial status epilepticus. Brain 128, 1369–1376.
Tak, A.Z.A., Şengül, Y., Ekmekçi, B., Karadağ, A.S., 2019. Comparison of optic coherence tomography results in patients with diagnosed epilepsy: findings in favor of neurodegeneration. Epilepsy Behav. 94, 313.
Trattnig, S., Springer, E., Bogner, W., Hangel, G., Strasser, B., Dymerska, B., Cardoso, P. L., Robinson, S.D., 2018. Key clinical benefits of neuroimaging at 7T. NeuroImage 168, 477–489.
Trinka, E., Cock, H., Hesdorffer, D., Rossetti, A.O., Scheffer, I.E., Shinnar, S., Shorvon, S., Lowenstein, D.H., 2015. A definition and classification of status epilepticus–Report of the ILAE Task Force on Classification of Status Epilepticus. Epilepsia 56, 1515–1523.
Vila Verde, D., Zimmer, T., Cattalini, A., Pereira, M.F., van Vliet, E.A., Testa, G., Gnatkovsky, V., Aronica, E., de Curtis, M., 2021. Seizure activity and brain damage in a model of focal non-convulsive status epilepticus. Neuropathol. Appl. Neurobiol.
Walker, M.C., 2007. Treatment of nonconvulsive status epilepticus. Int. Rev. Neurobiol. 81, 287–297.